# A multifunctional AAV–CRISPR–Cas9 and its host response

Wei Leong Chew[1,2,8], Mohammadsharif Tabebordbar[2,3,8], Jason K W Cheng[3], Prashant Mali[1,7], Elizabeth Y Wu[3,7], Alex H M Ng[1,4], Kexian Zhu[3,5], Amy J Wagers[3] & George M Church[1,6]

CRISPR–Cas9 delivery by adeno-associated virus (AAV) holds promise for gene therapy but faces critical barriers on account of its potential immunogenicity and limited payload capacity. Here, we demonstrate genome engineering in postnatal mice using AAV–split-Cas9, a multifunctional platform customizable for genome editing, transcriptional regulation, and other previously impracticable applications of AAV–CRISPR–Cas9. We identify crucial parameters that impact efficacy and clinical translation of our platform, including viral biodistribution, editing efficiencies in various organs, antigenicity, immunological reactions, and physiological outcomes. These results reveal that AAV–CRISPR–Cas9 evokes host responses with distinct cellular and molecular signatures, but unlike alternative delivery methods, does not induce extensive cellular damage *in vivo*. Our study provides a foundation for developing effective genome therapeutics.

The CRISPR–Cas9 system enables programmable genetic and epigenetic manipulations[1–3] that present exciting opportunities for personalized therapeutics. As CRISPR–Cas9 approaches the clinic, efficacy and safety for the patient are paramount. With this concern in mind, many have endeavored to deploy CRISPR–Cas9 with AAVs, delivery vectors that are prevalent, serologically compatible with a large fraction of the human population[4,5], and generally considered nonpathogenic. In addition, AAVs allow semiselective tissue tropism via local or systemic delivery[6]. We and others recently highlighted the preclinical promise of AAV–CRISPR–Cas9 for modification of inherited genetic defects in mice[7–12]. Further application of AAV–CRISPR–Cas9 for modulating postnatal chromatin status or gene expression would vest profound biological control, particularly in treating diseases resulting from epigenetic alterations irresolvable by genome editing. However, this ability has yet to be realized, in part because the large Cas9 transgenes leave little space for additional function-conferring elements within current designs[7–14] (AAV payload limit ≤ 4.7 kb). This obstacle is exacerbated by the size of the most widely used *Streptococcous pyogenes* Cas9 (SpCas9, 4.2 kb), which makes packaging of even the minimally functional cassette extremely challenging[10,13,14]. Hence, in this study, we sought to first establish a flexible AAV–CRISPR–Cas9 platform that enables the wide spectrum of unrealized applications *in vivo*. Second, we tracked how the host responded to our system. This is important because the exogenous nature of AAV–CRISPR–Cas9 might incite detrimental host reactions against the encoded transgenes and/or viral capsid (reviewed in ref. 15). Understanding the host responses toward AAV–CRISPR–Cas9 would identify confounding factors that impact experimental rigor, highlight relevant considerations for clinical translation, and provide a roadmap for engineering efficient genome manipulation systems.

## RESULTS

### Full activity and facile AAV packaging of split-Cas9

Of the various CRISPR–Cas9 (refs. 1–3,7,16) and recently characterized CRISPR–Cpf1 (ref. 17) orthologs, we chose to examine SpCas9 because it possesses multiple attractive features (see **Supplementary Note**). Most importantly, SpCas9 has the least restrictive protospacer adjacent motif (PAM) requirement among Cas9 orthologs, and thus provides the highest density of possible target sites per given genome (**Supplementary Fig. 1a**). Conversely, more restrictive PAM requirements (e.g., those of *Streptococcus thermophilus* (St1; ref. 16), *Neisseria meningitides* (Nm; ref. 16), and *Staphylococcus aureus* (Sa; ref. 7) Cas9s; and of *Acidaminococcus sp.* (As) and *Lachnospiraceae bacterium* (Lb) Cpf1s[17]) render many target sites inaccessible. SpCas9 also adopts a bilobed protein architecture[18,19] (similar to those of Sa (ref. 20) and *Actinomyces naeslundii* (Ana; ref.19) Cas9s but distinct from that of *Francisella novicida* (Fn; ref. 21) Cas9). We hypothesized that splitting SpCas9 at its disordered linker (V713–D718) would maintain protein folding for each lobe, allowing seamless reconstitution of full-length Cas9 (Cas9[FL]) *in vivo* by split-intein protein *trans*-splicing[22] (**Supplementary Fig. 1b**). This structure-guided design might be necessary because prior reports in cell cul-
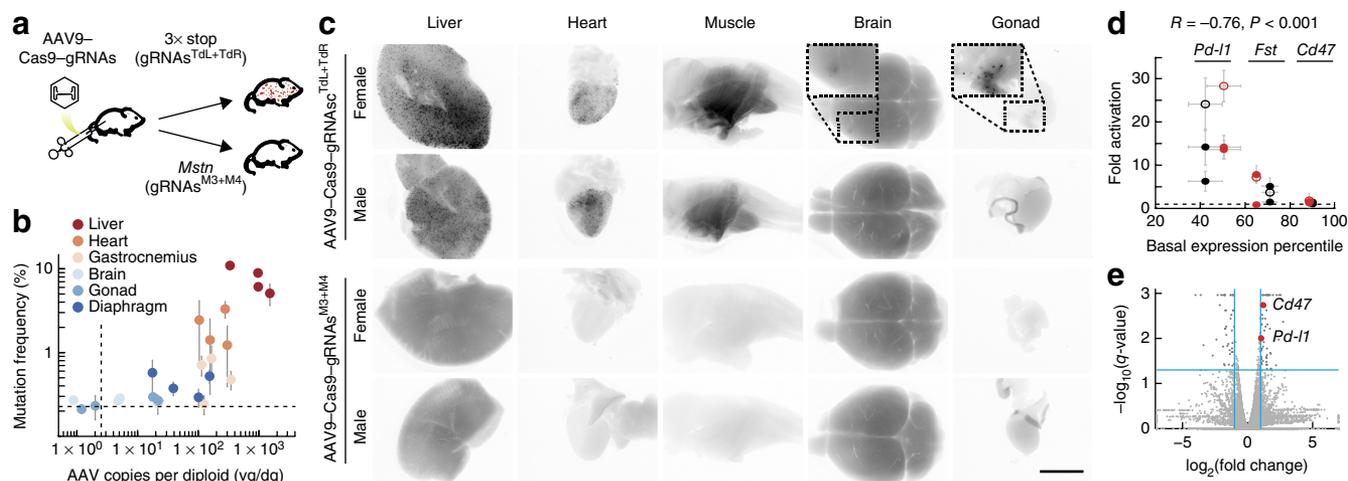
**Figure 1** | Postnatal genome editing with AAV9–Cas9–gRNAs and transcriptional activation with AAV9–Cas9–VPR–gRNAs. (**a**) AAV9–Cas9–gRNAs targeting the endogenous *Mstn* gene or the 3× stop cassette in neonatal mice. (**b**) Mutation frequency and AAV9 transduction efficiency (Pearson's $R = 0.73$, Spearman's $\rho = 0.74$, $P < 0.05$) ($n = 4$ mice, 4E12 vg of AAV9–Cas9–gRNAs$^{M3+M4}$). Horizontal dashed line, sequencing error rate; vertical dashed line, qPCR false-positive rate. Error bars denote s.e.m. for sequencing and qPCR replicates. (**c**) Fluorescent images of AAV9–Cas9–gRNA$^{TdL+TdR}$-edited tdTomato$^{+}$ cells in the indicated organs (2 upper rows, $n = 3$ total mice at $4 \times 10^{12}$ vg; 2 lower rows, $n = 4$ total mice at $4 \times 10^{12}$ vg). Gray, tdTomato. Scale bar, 5 mm. (**d**) AAV–Cas9–VPR–gRNA-mediated gene activation of the indicated genes in myotubes (black) and spermatogonial cells (red). Closed dots denote single gRNA, and open circles denote dual gRNAs (AAV–Cas9$^{N}$–gRNA:AAV–Cas9$^{C}$–VPR, 1:1). Error bars denote s.e.m. (**e**) AAV9–Cas9–VPR–gRNA-mediated gene activation in adult mice (false discovery rate (FDR) = 0.05). Volcano plot shows total mRNA sequencing of the same muscle samples used for qRT-PCR in **Supplementary Figure 7e** ($n = 3$ mice per condition).

tures[20,23–27], each with distinct design principles, have demonstrated that splitting Cas9 resolves its unwieldy size but often interferes with its function. Here, we fused the Cas9 N-terminal lobe with the *Rhodothermus marinus* N-split intein (Cas9$^{N}$; 2.5 kb) and the C-terminal lobe with C-split intein (Cas9$^{C}$; 2.2 kb), which shortened the coding sequences below those of all known Cas9 orthologs and liberated >2 kb in each AAV vector for additional elements. Split-Cas9 was fully active in transfected cells, targeting the endogenous genes tested at efficiencies equivalent to Cas9$^{FL}$ (**Supplementary Fig. 1c,d**). Full activity from structure-guided split-intein reconstitution[26] contrasts with suboptimal activity from noncovalent heterodimerization[20,23–25], suggesting that scarless protein ligation preserves Cas9 structure and function. Next, we packaged Cas9$^{C}$–P2A–turboGFP and Cas9$^{N}$–U6–gRNAs into AAV serotype DJ (AAV–Cas9–gRNAs) (**Supplementary Fig. 2a**) and applied the viruses to cultured cells. AAV–Cas9–gRNAs modified target genes in differentiated myotubes, tail-tip fibroblasts, and spermatogonial cells (**Supplementary Fig. 2b–f**), demonstrating robustness in three distinct cell types representing proliferative and terminally differentiated cell states.

### Delivery efficiency dictates genome-editing rate

To evaluate functionality *in vivo*, we next pseudotyped AAV–Cas9–gRNAs targeting *Mstn* to serotype 9 (AAV9–Cas9–gRNAs$^{M3+M4}$) and injected the viruses intraperitoneally into neonatal mice (5E11 or 4E12 vector genomes, vg) (**Fig. 1a**). Deep sequencing of whole tissues from injected mice revealed a range of editing frequencies (up to 10.9%) similar to those observed in cell culture (**Supplementary Figs. 1** and **2**) and in single myofibers following an alternative delivery method of intramuscular DNA electroporation (**Supplementary Fig. 3a**). Interestingly, editing frequencies exhibited intertissue bias for both on-target (*Mstn*) and off-target (chr16:+3906202) sites (**Supplementary Fig. 4a–c**), which correlated strongly with the concentrations of AAV9–Cas9–gRNAs

per cell (vector genomes per mouse diploid genome, vg/dg) (**Fig. 1b** and **Supplementary Fig. 4d–f**). This dose dependency indicates that delivery efficiency dictates editing rate, and despite sufficiency in titers for infecting most cells (**Supplementary Fig. 4g,h**), higher AAV9–Cas9–gRNAs copies per cell continue to increase editing frequencies. Next, to demarcate viral biodistribution, we tracked AAV9–Cas9–gRNAs activity at single-cell resolution using the Ai9 mouse line[28] that accurately couples genomic excision of a 3× stop cassette with tdTomato fluorescence activation (**Fig. 1a** and **Supplementary Fig. 3b–d**). Systemic delivery of AAV9–Cas9–gRNAs$^{TdL+TdR}$ (5E11 or 4E12 vg), targeting sequences flanking the 3× stop cassette, generated excision-dependent tdTomato$^{+}$ cells in all examined organs (**Fig. 1c**, **Supplementary Figs. 5** and **6**). These data demonstrate that the AAV–split-Cas9 platform is functional for genome editing of multiple organs.

### Split-Cas9 enables AAV delivery of Cas9 fusion proteins

We next capitalized on the additional viral capacity of AAV–split-Cas9 to incorporate transcription-activator fusion domains (Cas9$^{C}$ fused to the 1.6-kb tripartite VPR[29]) for targeted upregulation of gene expression (AAV–Cas9–VPR). We further made use of the fact that nuclease-active Cas9 programmed with truncated gRNAs can bind genomic loci without inducing DNA breaks, which allows use of a single Cas9-activator fusion protein for either gene editing or gene activation, depending on the gRNA spacer length[30,31]. However, AAV–Cas9–VPR programmed with full-length gRNAs targeting *Mstn* showed reduced endonucleolytic activity compared with AAV–Cas9 (**Supplementary Fig. 7a**). In contrast, the same nuclease-active AAV–Cas9–VPR, programmed with truncated gRNAs (14- to 15-nt spacers), upregulated gene expression of the target *Pd-l1* (*Cd274*), *Fst*, and *Cd47* genes (up to 23-, 9-, and 2-fold, respectively; **Fig. 1d** and **Supplementary Fig. 7b,c**). Gene activation by AAV–Cas9–VPR–gRNAs inversely correlated with the basal expression levels of the target genes,
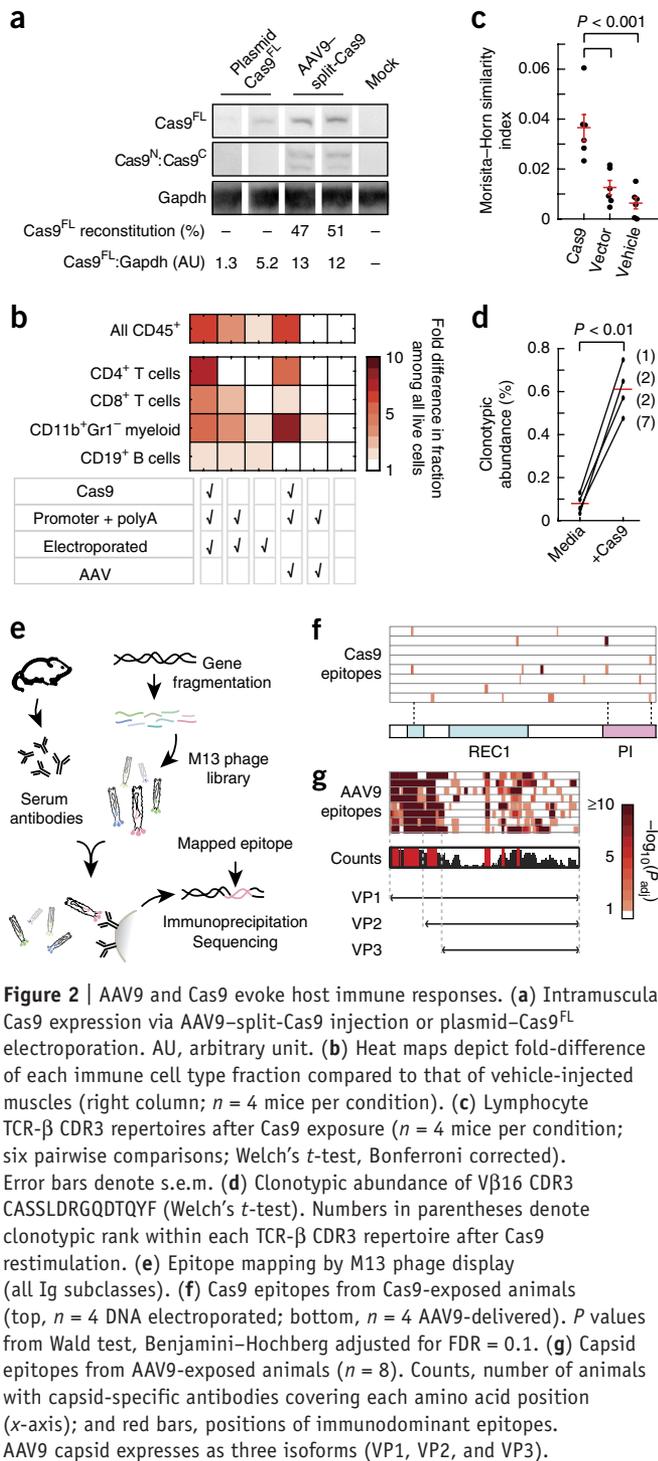
**Figure 2** | AAV9 and Cas9 evoke host immune responses. (**a**) Intramuscular Cas9 expression via AAV9–split-Cas9 injection or plasmid–Cas9[FL] electroporation. AU, arbitrary unit. (**b**) Heat maps depict fold-difference of each immune cell type fraction compared to that of vehicle-injected muscles (right column; $n = 4$ mice per condition). (**c**) Lymphocyte TCR-β CDR3 repertoires after Cas9 exposure ($n = 4$ mice per condition; six pairwise comparisons; Welch's $t$-test, Bonferroni corrected). Error bars denote s.e.m. (**d**) Clonotypic abundance of Vβ16 CDR3 CASSLDRGQDTQYF (Welch's $t$-test). Numbers in parentheses denote clonotypic rank within each TCR-β CDR3 repertoire after Cas9 restimulation. (**e**) Epitope mapping by M13 phage display (all Ig subclasses). (**f**) Cas9 epitopes from Cas9-exposed animals (top, $n = 4$ DNA electroporated; bottom, $n = 4$ AAV9-delivered). $P$ values from Wald test, Benjamini–Hochberg adjusted for FDR = 0.1. (**g**) Capsid epitopes from AAV9-exposed animals ($n = 8$). Counts, number of animals with capsid-specific antibodies covering each amino acid position ($x$-axis); and red bars, positions of immunodominant epitopes. AAV9 capsid expresses as three isoforms (VP1, VP2, and VP3).

potentially circumscribed by a bottleneck in the endogenous transcriptional machinery, a trend also observed with transfected nuclease-inactive 'dead' Cas9[FL] (dCas9)-activator plasmids[29,32]. Importantly, AAV–Cas9[FL]s are unable to accommodate the VPR domain fusion. Hence, split-Cas9 enables AAV delivery of engineered Cas9 fusion proteins.

## Postnatal gene activation with AAV9–Cas9–VPR–gRNAs
Next, we tested Cas9-mediated transcriptional regulation *in vivo*. Our initial comparison of samples treated with AAV9

–Cas9–VPR–gRNAs and AAV9–turboRFP (4E12 vg and 1E11 vg, respectively) against those with AAV9–turboRFP only (1E11 vg) could not be accurately analyzed amidst global transcriptome perturbations (**Supplementary Fig. 7d**), a host reaction that we describe in detail below. Hence, we focused on mice intramuscularly injected with equivalent dosages of AAV9–Cas9–VPR–gRNAs and AAV9–turboRFP, with only the gRNA spacer sequences varied to target different sets of genes. Compared with control mice injected with AAV9–Cas9–VPR–gRNAs targeting only *Mstn* and *Fst*, mice injected with AAV9–Cas9–VPR–gRNAs targeting *Mstn*, *Fst*, *Pd-l1*, and *Cd47* showed modest activation of the *Pd-l1* and *Cd47* genes (2.1-fold and 2.3-fold, respectively, as assessed by mRNA sequencing 2 weeks post-treatment) (**Fig. 1e** and **Supplementary Fig. 7e**). This result demonstrated, for the first time, postnatal transcriptional regulation with CRISPR–Cas9.

## Cas9 evokes cellular immune responses while AAV9 does not
The transcriptome perturbations observed alongside on-target gene activation provide a segue into our second aim, as these differentially expressed genes (>1,000 loci) were significantly enriched for a spectrum of immunological processes (**Supplementary Fig. 8** and **Supplementary Table 1**). This result places immunogenicity of AAV–CRISPR–Cas9 as a key property that destabilizes the host system, and could conceivably impact its use *in vivo*. To address this imminent concern, we proceeded to dissect the immunological response to AAV9–split-Cas9, in parallel with the alternative delivery method of intramuscular DNA electroporation (encoding Cas9[FL]). Regardless of delivery method, expression of Cas9 in the adult tibialis anterior muscle (**Fig. 2a** and **Supplementary Fig. 9a**) induced enlargement of the draining lymph nodes with increased cell counts (**Supplementary Fig. 9b**). In Cas9-expressing muscles, the frequencies of CD45+ hematopoietic cells were also significantly elevated (**Fig. 2b** and **Supplementary Fig. 9b**) and enriched around transgene-expressing myofibers (**Supplementary Fig. 9c**). Administering the same vectors without the Cas9 coding sequence did not elicit significant cellular infiltration or expansion, indicating a Cas9-driven immune response.

Within the expanded CD45+ population, myeloid cells (CD11b+Gr1− monocytes, macrophages, and/or dendritic cell subsets) and T cells (CD3+CD4+ and CD3+CD8+) were particularly enriched (**Fig. 2b** and **Supplementary Fig. 9d**–**f**). T cells orchestrate antigen-specific immune responses, with each clonal lineage expressing a unique T-cell receptor β-chain (TCR-β) CDR3 motif that mediate most of the antigen contact. The unique 'barcodes' of T-cell clonotypes allowed us to identify Cas9-responsive T cells through deep sequencing the TCR-β repertoires. We observed that Cas9 exposure skewed expansion of T-cell clonotypic subsets (**Fig. 2c**), which implied antigen-specific T-cell activation and proliferation. Four TCR-β clonotypes were common to all Cas9-exposed animals ($n = 4$) and undetected in all unexposed animals ($n = 8$). Because bona fide T cells would proliferate with antigen recall, we sought to confirm antigen-specific T-cell expansion by challenging extracted lymphocytes with purified Cas9 protein. Of the four initial clonotypes, we identified one (Vβ16, CDR3: CASSLDRGQDTQYF) as a true Cas9-responsive T-cell clonotype, which proliferated according to Cas9 protein restimulation (**Fig. 2d**). Hence, Cas9 activates a cellular immune
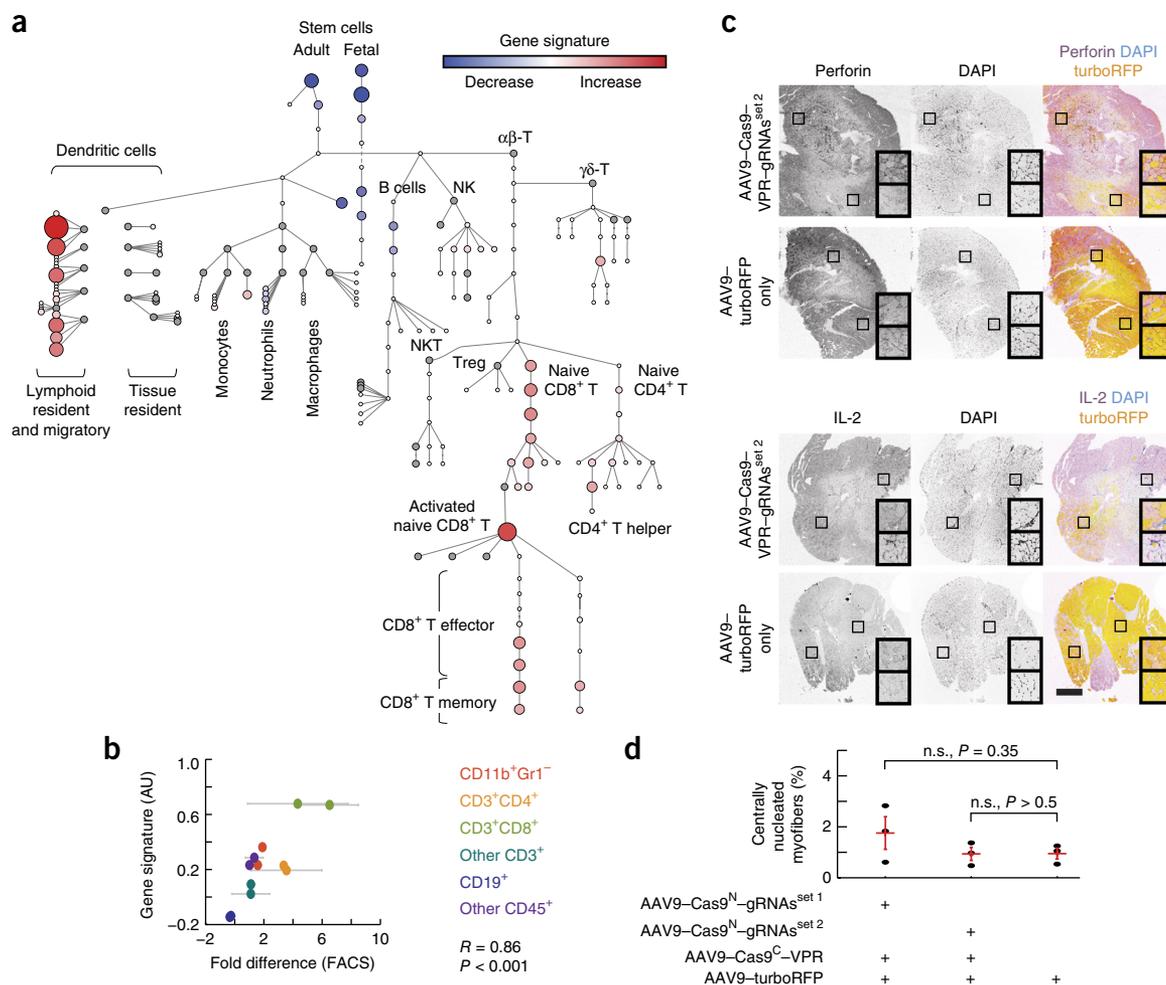
**Figure 3** | Immunological phenotypes toward AAV–CRISPR–Cas9. (**a**) Deconvoluted hematopoietic lineage tree from muscle samples. Node sizes scale with fold-differences in gene signatures induced by AAV9–Cas9–VPR–gRNA$^{set\ 2}$ treatment ($n$ = 3 mice per condition). Detailed annotations are available in **Supplementary Figure 11**. (**b**) Cellular compositions determined by deconvolution reflect fractions quantified by FACS. Two groups of AAV9–Cas9–VPR–gRNAs-injected mice were compared to AAV9-turboRFP-injected negative control mice ($n$ = 3 mice per condition). Error bars denote within-group s.e.m. (**c**) Tissue sections immunostained for the indicated proteins in muscles injected with AAV9–Cas9–VPR–gRNAs ($4 \times 10^{12}$ vg; $n$ = 3 mice per condition). All injections included $1 \times 10^{11}$ vg of AAV9–turboRFP to demarcate transduction. Additional data are presented in **Supplementary Figure 12**. Scale bar, 500 μm. (**d**) Quantification of the fraction of centrally nucleated myofibers ($n$ = 3 mice per condition; one-way ANOVA, followed by Dunnett's test against mice injected with $1 \times 10^{11}$ vg of AAV9–turboRFP). n.s., not significant.

response, with at least one antigen-specific T-cell clonotype common among injected mice (suggestive of a public response), and with the other infiltrating T cells largely dissimilar between individuals (private response).

## Cas9 evokes humoral immune responses

Cas9-specific antibodies were also elicited postexposure, as confirmed by ELISA (**Supplementary Fig. 10a**). Individual mice exhibited variable titers of Cas9-specific antibodies, suggesting a largely private humoral response. To map Cas9 epitopes, serum from each animal was coincubated with M13 phage display libraries tiling the Cas9 transgene, and antibody targets were determined by Ig:phage pull down (**Fig. 2e** and **Supplementary Fig. 10b**). Epitope mapping showed that individual Cas9-exposed animals exhibited an antibody repertoire targeting unique residues of Cas9, but three linear epitopes were observed more than once (**Fig. 2f**, **Supplementary Fig. 10c**, and **Supplementary Table 2**). 1352-ITGLYETRI-1360 consists of residues recognizing gRNA

stem loop 2 (ref. 18); 122-IVDEVAYHEKYP-133 resides in the REC1 domain that contributes to Cas9:gRNA interactions, but the epitope does not include residues mediating the contact[18]. 1126-WDPKKYGGFD-1135 resides in the PAM-binding loop and contains conserved residues, but maintains Cas9 endonucleolytic function when selectively mutated (1125-DWD→AAA (ref. 19) or D1135E (ref. 33) for increasing Cas9 specificity). The combination of these residue changes retained Cas9 activity (**Supplementary Fig. 10d**). While speculative, future large-scale functional variant profiling could reveal more residues amenable to epitope recoding.

## AAV9 evokes humoral immune responses

In contrast to Cas9, AAV9 elicited capsid-specific antibodies (**Supplementary Fig. 10e**) against epitopes that were shared among injected animals at surprisingly high degrees (**Fig. 2g** and **Supplementary Table 2**), reminiscent of a public response to viruses recently observed also in humans[34]. Epitope mapping

provides intriguing support that AAV9 antigenicity derives from biophysical and functional aspects instead of purely sequence-level motifs. The metastable VP1 unique and VP1/2 common regions are antigenic, suggesting their externalization from the viral interior for antigen capture. Immunodominant epitopes in VP3 are over-represented on the capsid surface (**Supplementary Fig. 10f**). Notably, while many of these residues can be separately double-alanine mutated without disrupting viral assembly[35], they are predominantly implicated[35] in maintaining viral blood persistency (**Supplementary Fig. 10g**) and liver-selective tropism (**Supplementary Fig. 10h**). Together, the immunodominant VP3 epitopes (372-FMIPQYGYLTLNDGSQAVG-390, 436-MNPLIDQYLY-445, and 494-TQNNNSEFAWPG-505) cover 12 out of the 18 residues associated with AAV9 hepatotropism. Hence, AAV9 elicits humoral immunity that overlaps among animals across substantial regions of the capsid protein that modulate viral biodistribution.

### Transcriptome signatures following AAV–CRISPR–Cas9 exposure

Having established that AAV–CRISPR–Cas9 activates host immunity, we next investigated the associated functional impact of activating the host immune system. We returned to the total mRNA sequencing data, and by using the DCQ algorithm[36] against reference gene expression profiles derived by the Immunological Genome Project (ImmGen), we deconvoluted the admixture transcriptomes into >200 immune cell types of the hematopoietic lineage tree (**Fig. 3a**, **Supplementary Fig. 11**, and **Supplementary Table 3**). This deconvolution identified cell-type compositions concordant with bulk fractions quantified via FACS (**Fig. 3b**), but it afforded higher inferential power for generating testable hypotheses. First, gene signatures for differentiated B cells, monocytes, and dendritic cells were over-represented in the draining lymph nodes (**Supplementary Fig. 11a**), consistent with the observed humoral response and expected physiological niche. Second, in muscles treated with AAV9–Cas9–VPR–gRNAs, gene signatures for subsets of dendritic cells and T cells were dominant (**Fig. 3a**).

The presence of CD8+ T cells in Cas9-expressing tissues is particularly intriguing, because mature antigen-specific CD8+ T cells can induce tissue damage by cytolysis; however, from our data set we detected gene signatures that assigned the CD8+ lineage predominantly in the naïve or activated yet immature cell fates (**Fig. 3a**). A closer look at genes encoding key cytolytic T-cell differentiation signals (for example, *Il12*, *Ifn-α/β* (*Ifna* and *Ifnb1*), *Il2*, *Tbx21*, and *Eomes*) and cytolytic effector proteins (e.g., *Prf1*, *Gzmb*, and *Fasl*) revealed that these genes were not altered at statistically significant levels 2 weeks post-treatment (**Supplementary Table 1**). This led us to examine functional readouts more sensitively by intratissue immunofluorescence and histology.

### AAV–CRISPR–Cas9 does not evoke extensive cellular damage

Interleukin-2 (IL-2) is pivotal for cytolytic T-cell differentiation[37]. Downstream, perforin (Prf1) is the essential pore-forming protein released by cytolytic T lymphocytes and natural killer (NK) cells to destroy target cells. In line with mRNA sequencing, immunofluorescence indicated basal IL-2 and perforin protein levels within muscles treated with AAV9–Cas9–VPR–gRNAs, except for in sparse interstitial areas that corresponded to the highest density of cellular infiltrates (**Fig. 3c** and **Supplementary Fig. 12**).

The unremarkable perforin levels suggested minimal downstream cytolysis. To quantitatively assess cellular damage, we quantified the fraction of centrally nucleated myofibers within muscle histological sections, a physiological measure indicative of myofiber degeneration and repair. Through this assay, we did not observe significant muscle cell damage and repair responses at 2 weeks after administration of AAV9–Cas9–VPR–gRNAs (**Fig. 3d**). As positive controls for our assays, we examined muscles electroporated with DNA encoding Cas9FL. In contrast, IL-2 and perforin levels were both strongly increased in muscles 2 weeks after electroporation of Cas9-encoding DNA, and significant myofiber degeneration–repair was observed (**Supplementary Figs. 13** and **14a**). These observations following DNA electroporation could not simply be attributed to physical disruptions, because transgene-induced intramuscular CD45+ cellular infiltration, IgG and IgM antibody levels, IL-2 and perforin levels, and myofiber degeneration–repair (**Supplementary Figs. 13** and **14a–d**) were significantly elevated over vehicle-electroporated control mice and could be partially reduced by immunosuppression (FK506). Hence, our assays, which are adequately sensitive for detecting the extensive myofiber cytolysis evoked by electroporation of Cas9-encoding DNA, did not indicate significant myofiber damage and replacement after treatment with AAV9–Cas9–VPR–gRNAs.

### DISCUSSION

The use of CRISPR–Cas9 for research purposes and its and eventual clinical implementation require comprehensive evaluation of its *in vivo* profile, including its potential to evoke deleterious host responses. Delivery methods such as DNA electroporation and adenoviruses[38] cause severe inflammation and immunological reactions. Immunosuppression could arguably mitigate some of these detrimental consequences, but nonetheless is still associated with well-appreciated side effects (**Supplementary Fig. 14e**). Thus, more immunologically inert delivery vectors are particularly attractive. Precedents of immune evasion or tolerance induction by viruses have been documented in natural and experimental settings[15,39,40] and have fuelled ongoing efforts toward understanding and reducing the risk profiles of therapeutic vectors. Here, we contribute by directly interrogating the *in vivo* profile of AAV–CRISPR–Cas9, specifically that of our platform that allows flexible incorporation of function-conferring domain fusions that AAV–Cas9FLs cannot accommodate in their current forms[7–14] (**Supplementary Note**). We established on multiple fronts that AAV–CRISPR–Cas9 activated the immune system but had difficulty detecting muscle cell damage and repair responses with adequately sensitive assays in the timeframe of our experiments. We cannot rule out that immunological cytotoxicity could be tissue context specific, but this is unlikely to affect our conclusion because prior reports suggest that the muscle is more susceptible to cytolytic responses than are organs such as the liver[15]. Another caveat is in our use of wild-type mice for platform characterization, animals with immunological features that may differ in important ways from those of human subjects, especially in the inflammatory and procytotoxic disease contexts where AAV–CRISPR–Cas9 therapeutics might most readily be employed[41]. Interestingly, prior reports have shown that delivery of other transgenes with AAV also activates CD8+ T cells lacking full functionality, with these transgene-specific CD8+ T cells exhibiting impaired cytolytic activity[42] or cell viability[43].

It is here that further investigation toward bridging these two implications of our system—immune activation and undetected cellular damage—could reveal elements that may illuminate ways to further minimize its immunogenicity. In addition, whether the host immune response to AAV–CRISPR–Cas9 may impact other aspects of its therapeutic implementation, such as the effects toward on- and off-target gene modification and activity, remains an important topic for future investigation. In subsequent studies, the Cas9-reponsive T-cell clonotype identified here could serve as a distinctive biomarker for Cas9-specific immunity. On a parallel front, additional targeted engineering of AAV–CRISPR–Cas9 could be highly fruitful in defusing unintended side effects that remain prominent, bringing us toward a genome manipulation tool that is efficacious on target and inert otherwise. Cellular and molecular dissection of the host responses evoked by AAV–CRISPR–Cas9, as reported here, should aid in such efforts.

## METHODS

Methods and any associated references are available in the online version of the paper.

**Accession codes.** Deep sequencing data are available at Sequence Read Archive accession number SRP057723 under BioProject accession number PRJNA280362, and mRNA-sequencing data are available at Gene Expression Omnibus GSE84534. Plasmids are available through Addgene (IDs 80930–80944).

*Note: Any Supplementary Information and Source Data files are available in the online version of the paper.*

### AUTHOR CONTRIBUTIONS
W.L.C., M.T., A.J.W., and G.M.C. conceived of and designed the study and interpreted results. W.L.C. conducted *in vitro* experiments, viral production, mouse handling, genotyping, qPCR, western blot, TCR-β clonotyping, epitope mapping, fluorescent immunoassay, histology, immunostaining, microscopy, mRNA sequencing, and data analyses. M.T. conducted mouse handling, intramuscular electroporation, single myofiber isolation, FACS and its analysis, ELISA and its analysis, histology, and immunostaining. P.M. assisted in initial *in vitro* CRISPR–Cas9 optimization. J.K.W.C. and E.Y.W. conducted mouse handling, histology, and immunostaining. A.H.M.N. conducted mRNA sequencing and its analysis. K.Z. conducted mouse handling. W.L.C. wrote the manuscript with input from the other authors. G.M.C. and A.J.W. supervised the project and edited the manuscript.

### COMPETING FINANCIAL INTERESTS
The authors declare competing financial interests: details are available in the online version of the paper.

Reprints and permissions information is available online at http://www.nature.com/reprints/index.html.

1. Mali, P. *et al.* RNA-guided human genome engineering via Cas9. *Science* **339**, 823–826 (2013).
2. Cong, L. *et al.* Multiplex genome engineering using CRISPR/Cas systems. *Science* **339**, 819–823 (2013).
3. Jinek, M. *et al.* A programmable dual-RNA-guided DNA endonuclease in adaptive bacterial immunity. *Science* **337**, 816–821 (2012).
4. Gao, G. *et al.* Clades of adeno-associated viruses are widely disseminated in human tissues. *J. Virol.* **78**, 6381–6388 (2004).
5. Boutin, S. *et al.* Prevalence of serum IgG and neutralizing factors against adeno-associated virus (AAV) types 1, 2, 5, 6, 8, and 9 in the healthy population: implications for gene therapy using AAV vectors. *Hum. Gene Ther.* **21**, 704–712 (2010).
6. Zincarelli, C., Soltys, S., Rengo, G. & Rabinowitz, J.E. Analysis of AAV serotypes 1-9 mediated gene expression and tropism in mice after systemic injection. *Mol. Ther.* **16**, 1073–1080 (2008).
7. Ran, F.A. *et al.* *In vivo* genome editing using *Staphylococcus aureus* Cas9. *Nature* **520**, 186–191 (2015).
8. Nelson, C.E. *et al.* *In vivo* genome editing improves muscle function in a mouse model of Duchenne muscular dystrophy. *Science* **351**, 403–407 (2016).
9. Tabebordbar, M. *et al.* *In vivo* gene editing in dystrophic mouse muscle and muscle stem cells. *Science* **351**, 407–411 (2016).
10. Long, C. *et al.* Postnatal genome editing partially restores dystrophin expression in a mouse model of muscular dystrophy. *Science* **351**, 400–403 (2016).
11. Yang, Y. *et al.* A dual AAV system enables the Cas9-mediated correction of a metabolic liver disease in newborn mice. *Nat. Biotechnol.* **34**, 334–338 (2016).
12. Yin, H. *et al.* Therapeutic genome editing by combined viral and non-viral delivery of CRISPR system components *in vivo*. *Nat. Biotechnol.* **34**, 328–333 (2016).
13. Senís, E. *et al.* CRISPR/Cas9-mediated genome engineering: an adeno-associated viral (AAV) vector toolbox. *Biotechnol. J.* **9**, 1402–1412 (2014).
14. Swiech, L. *et al.* *In vivo* interrogation of gene function in the mammalian brain using CRISPR-Cas9. *Nat. Biotechnol.* **33**, 102–106 (2015).
15. Mays, L.E. & Wilson, J.M. The complex and evolving story of T cell activation to AAV vector-encoded transgene products. *Mol. Ther.* **19**, 16–27 (2011).
16. Esvelt, K.M. *et al.* Orthogonal Cas9 proteins for RNA-guided gene regulation and editing. *Nat. Methods* **10**, 1116–1121 (2013).
17. Zetsche, B. *et al.* Cpf1 is a single RNA-guided endonuclease of a class 2 CRISPR-Cas system. *Cell* **163**, 759–771 (2015).
18. Nishimasu, H. *et al.* Crystal structure of Cas9 in complex with guide RNA and target DNA. *Cell* **156**, 935–949 (2014).
19. Jinek, M. *et al.* Structures of Cas9 endonucleases reveal RNA-mediated conformational activation. *Science* **343**, 1247997 (2014).
20. Nishimasu, H. *et al.* Crystal structure of *Staphylococcus aureus* Cas9. *Cell* **162**, 1113–1126 (2015).
21. Hirano, H. *et al.* Structure and engineering of *Francisella novicida* Cas9. *Cell* **164**, 950–961 (2016).
22. Li, J., Sun, W., Wang, B., Xiao, X. & Liu, X.Q. Protein *trans*-splicing as a means for viral vector-mediated *in vivo* gene therapy. *Hum. Gene Ther.* **19**, 958–964 (2008).
23. Zetsche, B., Volz, S.E. & Zhang, F. A split-Cas9 architecture for inducible genome editing and transcription modulation. *Nat. Biotechnol.* **33**, 139–142 (2015).
24. Wright, A.V. *et al.* Rational design of a split-Cas9 enzyme complex. *Proc. Natl. Acad. Sci. USA* **112**, 2984–2989 (2015).
25. Nihongaki, Y., Kawano, F., Nakajima, T. & Sato, M. Photoactivatable CRISPR-Cas9 for optogenetic genome editing. *Nat. Biotechnol.* **33**, 755–760 (2015).
26. Truong, D.J. *et al.* Development of an intein-mediated split-Cas9 system for gene therapy. *Nucleic Acids Res.* **43**, 6450–6458 (2015).
27. Fine, E.J. *et al.* *Trans*-spliced Cas9 allows cleavage of HBB and CCR5 genes in human cells using compact expression cassettes. *Sci. Rep.* **5**, 10777 (2015).
28. Madisen, L. *et al.* A robust and high-throughput Cre reporting and characterization system for the whole mouse brain. *Nat. Neurosci.* **13**, 133–140 (2010).
29. Chavez, A. *et al.* Highly efficient Cas9-mediated transcriptional programming. *Nat. Methods* **12**, 326–328 (2015).
30. Kiani, S. *et al.* Cas9 gRNA engineering for genome editing, activation and repression. *Nat. Methods* **12**, 1051–1054 (2015).
31. Dahlman, J.E. *et al.* Orthogonal gene knockout and activation with a catalytically active Cas9 nuclease. *Nat. Biotechnol.* **33**, 1159–1161 (2015).
32. Konermann, S. *et al.* Genome-scale transcriptional activation by an engineered CRISPR-Cas9 complex. *Nature* **517**, 583–588 (2015).
33. Kleinstiver, B.P. *et al.* Engineered CRISPR-Cas9 nucleases with altered PAM specificities. *Nature* **523**, 481–485 (2015).

34. Xu, G.J. *et al.* Viral immunology. Comprehensive serological profiling of human populations using a synthetic human virome. *Science* **348**, aaa0698 (2015).

35. Adachi, K., Enoki, T., Kawano, Y., Veraz, M. & Nakai, H. Drawing a high-resolution functional map of adeno-associated virus capsid by massively parallel sequencing. *Nat. Commun.* **5**, 3075 (2014).

36. Altboum, Z. *et al.* Digital cell quantification identifies global immune cell dynamics during influenza infection. *Mol. Syst. Biol.* **10**, 720 (2014).

37. Pipkin, M.E. *et al.* Interleukin-2 and inflammation induce distinct transcriptional programs that promote the differentiation of effector cytolytic T cells. *Immunity* **32**, 79–90 (2010).

38. Wang, D. *et al.* Adenovirus-mediated somatic genome editing of *Pten* by CRISPR/Cas9 in mouse liver in spite of Cas9-specific immune responses. *Hum. Gene Ther.* **26**, 432–442 (2015).

39. Zajac, A.J. *et al.* Viral immune evasion due to persistence of activated T cells without effector function. *J. Exp. Med.* **188**, 2205–2213 (1998).

40. Curtsinger, J.M., Lins, D.C. & Mescher, M.F. Signal 3 determines tolerance versus full activation of naive CD8 T cells: dissociating proliferation and development of effector function. *J. Exp. Med.* **197**, 1141–1151 (2003).

41. Mendell, J.R. *et al.* Dystrophin immunity in Duchenne's muscular dystrophy. *N. Engl. J. Med.* **363**, 1429–1437 (2010).

42. Lin, S.W., Hensley, S.E., Tatsis, N., Lasaro, M.O. & Ertl, H.C. Recombinant adeno-associated virus vectors induce functionally impaired transgene product-specific CD8+ T cells in mice. *J. Clin. Invest.* **117**, 3958–3970 (2007).

43. Velazquez, V.M., Bowen, D.G. & Walker, C.M. Silencing of T lymphocytes by antigen-driven programmed death in recombinant adeno-associated virus vector-mediated gene therapy. *Blood* **113**, 538–545 (2009).

## ONLINE METHODS

**Constructs and sequences.** U6-driven gRNA plasmids were constructed as described[1]. AAV plasmid backbone was derived from pZac2.1–CASI–EGFP–RGB, a gift from Luk Vandenberghe (Schepens Eye Research Institute and Massachusetts Eye and Ear Infirmary). Minicircles parental plasmids were cloned in ZYCY10P3S2T, and minicircles were generated as described[44]. AAV plasmids were cloned in Stbl3 (Life Technologies C7373-03). All other plasmids were cloned in DH5α (NEB C2987H). Protein transgenes were expressed from ubiquitous hybrid promoters: SMVP promoter (generated by fusing SV40enhancer–CMV–promoter–chimeric intron), CASI promoter[45], or CAG promoter[46]. SMVP plasmid was derived from pMAXGFP (Lonza). pCAG–GFP was a gift from Connie Cepko (Harvard Medical School, Addgene plasmid no. 11150). pAAV–CMV–HI–eGFP–Cre–WPRE–SV40pA was obtained from the University of Pennsylvania Vector Core. Sequences of gRNA spacers, genotyping primers, qPCR probes and primers are stated in **Supplementary Table 4**. Sequences of split-Cas9 are stated in **Supplementary Sequence**.

**AAV packaging and purification.** AAVs were packaged via the triple-transfection method[47,48]. HEK293 cells (Cell Biolabs AAV-100 or Agilent 240073) were plated in growth media consisting of DMEM + glutaMAX + pyruvate + 10% fetal bovine serum (FBS) (Life Technologies) supplemented with 1× MEM nonessential amino acids (Gibco). Confluency at transfection was between 70% and 90%. Media was replaced with fresh prewarmed growth media before transfection. For each 15-cm dish, 20 μg of pHelper (Cell Biolabs), 10 μg of pRepCap (encoding capsid proteins for AAV-DJ (Cell Biolabs) or AAV9 (UPenn Vector Core)), and 10 μg of pAAV were mixed in 500 μl of DMEM, and 200 μg of PEI 'MAX' (Polysciences) (40 kDa, 1 mg/ml in H$_2$O, pH 7.1) added for PEI:DNA mass ratio of 5:1. The mixture was incubated for 15 min and transferred dropwise to the cell media. For large-scale AAV production, HYPERFlask 'M' (Corning) was used, and the transfection mixture consisted of 200 μg of pHelper, 100 μg of pRepCap, 100 μg of pAAV, and 2 mg of PEIMAX. The day after transfection, media was changed to DMEM + glutamax + pyruvate + 2% FBS. Cells were harvested 48–72 h after transfection by scrapping or dissociation with 1× PBS (pH7.2) + 5 mM EDTA, and they were pelleted at 1,500 g for 12 min. Cell pellets were resuspended in 1–5 ml of lysis buffer (Tris HCl pH 7.5 + 2 mM MgCl + 150 mM NaCl), and freeze–thawed 3 times between dry-ice-ethanol bath and 37 °C water bath. Cell debris was clarified via 4,000 g for 5 min, and the supernatant was collected. Downstream processing differed depending on applications.

For preparation of AAV-containing lysates, the collected supernatant was treated with 50 U/ml of Benzonase (Sigma-Aldrich) and 1 U/ml of Riboshredder (Epicentre) for 30 min at 37 °C to remove unpackaged nucleic acids, filtered through a 0.45 μm PVDF filter (Millipore), and used directly on cells or stored at −80 °C.

For purification of AAV via chloroform–ammonium sulfate precipitation, 0.10 volume of chloroform and NaCl (1 M final concentration) was added to the lysate and shaken vigorously. After centrifugation, the supernatant was incubated with PEG-8000 (10% final w/v) on ice for ≥1 h or overnight. PEG-precipitated virions were centrifuged (4,000g, 30 min, 4 °C), and resuspended in 50 mM HEPES buffer (pH 8). 50 U/ml of benzonase (Sigma-Aldrich)

and 1 U/ml of Riboshredder (Epicentre) were added and incubated for 30 min at 37 °C. An equal volume of chloroform was then added, and the mixture was vigorously vortexed. After centrifugation, the aqueous phase was collected and residual chloroform evaporated for 30 min. Ammonium sulfate precipitation of AAVs was performed with a 0.5 M to 2 M cutoff. AAVs were then resuspended and dialyzed in 1× PBS + 35 mM NaCl, quantified for viral titers, and stored in −80 °C.

All experiments with purified AAVs used the iodixanol density gradient ultracentrifugation purification method[47,48] unless otherwise stated. The collected AAV supernatant was first treated with 50 U/ml benzonase and 1 U/ml Riboshredder for 30 min at 37 °C. After incubation, the lysate was concentrated to <3 ml by ultrafiltration with Amicon Ultra-15 (50 kDa MWCO; Millipore) and loaded on top of a discontinuous density gradient consisting of 2 ml each of 15%, 25%, 40%, and 60% Optiprep (Sigma-Aldrich) in an 11.2 ml Optiseal polypropylene tube (Beckman–Coulter). The tubes were ultracentrifuged at 58,000 r.p.m. at 18 °C for 1.5 h on an NVT65 rotor. The 40% fraction was extracted and dialyzed with 1× PBS (pH 7.2) supplemented with 35 mM NaCl using Amicon Ultra-15 (50 kDa or 100 kDa MWCO; Millipore). The purified AAVs were quantified for viral titers and stored in −80 °C.

AAV2/9–CMV–HI–eGFP–Cre–WPRE–SV40 (Lot V4565MI-R), AAV2/9–CB7–CI–eGFP–WPRE–rBG (lot CS0516(293)), AAV2/9–CB7–CI–mCherry–WPRE–rBG (lot V4571MI-R), and AAV2/9–CMV–turboRFP–WPRE–rBG (lot V4528MI-R-DL) were obtained from the University of Pennsylvania Vector Core.

AAV titers (vector genomes) were quantified via hydrolysis–probe qPCR[49] against standard curves generated from linearized parental AAV plasmids.

**Cell culture transfection and transduction.** All cells were incubated at 37 °C and 5% CO$_2$.

C2C12 cells were obtained from the American Tissue Collection Center (ATCC, Manassas, VA) and grown in growth media (DMEM + glutaMAX + 10% FBS). Cells were split with TypLE Express (Invitrogen) every 2–3 d and before reaching 80% confluency to prevent terminal differentiation. Passage number was kept below 15. For transfection of C2C12 myoblasts, 10$^5$ cells were plated per well in a 24-well plate in 500 μl of growth media. The following day, fresh media was replaced, and 800 ng of total plasmid DNA was transfected with 2.4 μl of Lipofectamine 2000 (Life Technologies). 1:1 mass ratio of vectors encoding Cas9:gRNA(s) was used. Media was replaced with differentiation media (DMEM + glutaMAX + 2% donor horse serum) 1 and 3 d postlipofection.

For differentiation of C2C12 into myotubes, 2 × 10$^4$ cells were plated per well in a 96-well plate in 100 μl of growth media. At confluency, 1–2 d after plating, media was replaced with fresh differentiation media (DMEM + glutaMAX + 2% donor horse serum) and further incubated for 4 d. Fresh differentiation media was replaced before transduction with AAVs. Culture media was replaced with fresh differentiation media 1d after transduction, and cells were incubated for stated durations.

The 3× stop-tdTomato reporter cell line was derived from tail-tip fibroblasts of Ai9 (ref. 28) mouse (JAX No. 007905) and immortalized with lentiviruses encoding the large SV40 T antigen (GenTarget Inc., LVP016-Puro). Cells were cultured in DMEM + pyruvate + glutaMAX + 10% FBS. Lipofectamine 2000 (Life Technologies) was used for transfection of plasmids, and images

were taken 5 d after transfection. For transduction with AAVs, cells were plated at $2 \times 10^4$ per well in a 96-well plate in 100 µl of growth media. AAV-containing lysates or purified AAVs were applied at confluency of 70–90%. Culture media was replaced with fresh growth media the next day, and cells were incubated for stated durations.

The GC-1 spg mouse spermatogonial cell line (CRL-2053) was obtained from ATCC. Cells were cultured and transduced similarly to the 3× stop-tdTomato cell line with a Cas9$^N$:Cas9$^C$ of 1:1.

Cell lines were not tested for mycoplasma contamination after commercial purchase or primary isolation.

**Animals.** All animal procedures were approved by the Harvard University Institutional Animal Care and Use Committee.

Ai9 (ref. 28) mice (JAX No. 007905) were used for tdTomato activation and for systemic AAV9–Cas9–gRNAs and AAV9–GFP–Cre experiments, randomized at approximately 50:50 male:female ratios, with sex of each animal depicted in the figures. C57BL/6 male mice were used for *in vivo* electroporation and intramuscular AAV injections.

Standard sample sizes were chosen for all experiments. Exact sample sizes for experiments are stated in figure legends and text. Statistical methods were not used for predetermination of power. All animals were randomly allocated to treatment and control groups and handled equally.

***In vivo* electroporation.** Animals were anesthetized using isoflurane and injected with 50 µl of 2 mg/ml hyaluronidase (Sigma-Aldrich, H4272) in the tibialis anterior muscle. After 1 h, plasmids in vehicle (10 mM Tris–HCl, pH 8.0) were injected into the muscle, followed by electroporation[50] (10 pulses of 20 ms at 100 V/cm with 100 ms intervals) using an ECM 830 Electro Square Porator (BTX Harvard Apparatus) and a two-needle array.

For Ai9 reporter activation, 30 µg of pSMVP–SpCas9$^{FL}$, 60 µg total of pCRII–U6–gRNA, and 15 µg of pCAG–GFP were used for CRISPR–Cas9 injections; 30 µg of pSMVP–Cre and 15 µg of pCAG–GFP were used for Cre injections; and 30 µg of pSMVP–SpCas9$^{FL}$ and 15 µg of pCAG–GFP were used for no-gRNA control injections. FK506 (Sigma-Aldrich, F4679) was administered daily at 5 mg/kg (body weight), commencing 1 d before electroporation.

For C57BL/6 gene-targeting, 30 µg of vectors encoding SpCas9$^{FL}$ (pSMVP–SpCas9 or minicircle–SMVP–SpCas9), 30 µg total of pCRII–U6–gRNA, and 15 µg of pCAG–GFP were used. With cotranslating P2A–turboGFP, pCAG–GFP was omitted, and 30 µg pSMVP–SpCas9–P2A–turboGFP and 30 µg total of pCRII–U6–gRNA were used.

For immunogenicity comparison to AAV–split-Cas9, both tibialis anterior muscles of 11-week-old male C57BL/6 mice were each electroporated with 30 µg of pSMVP–Cas9$^{FL}$. Control mice were electroporated with 30 µg of plasmid vector control (consisting of the same plasmid with Cas9 coding sequence removed) per muscle. Vehicle electroporations were similarly performed. Animals were euthanized via $CO_2$ asphyxia and cervical dislocation 2 weeks after treatment.

**Single myofiber isolation.** Mice were euthanized via $CO_2$ asphyxia and cervical dislocation 10 d after *in vivo* electroporation.

Dissected muscles were digested with 0.2% collagenase type II in DMEM for 50 min at 37 °C. Muscles were triturated with fire-polished Pasteur pipettes and single GFP$^+$ myofibers isolated under a SMZ1500 (Nikon) fluorescence dissection stereomicroscope.

**Genotyping and analysis.** C2C12 cells were harvested 4 d postlipofection with 100 µl of QuickExtract DNA Extraction Solution (Epicentre) per well of a 24-well plate; and C2C12 myotubes were harvested 7 d post-AAV transduction with 20 µl of DNA QuickExtract per well of a 96-well plate. Cell lysates were heated at 65 °C for 10 min and 95 °C for 8 min, and they were stored at −20 °C. Each locus was amplified from 0.5 µl of cell culture lysate per 25 µl PCR reaction, for 20–25 cycles.

Single myofibers were each placed in 10 µl of QuickExtract DNA Extraction Solution and heated at 65 °C for 15 min and 95 °C for 10 min. For genotyping, the entire lysate was used in a 100 µl PCR reaction and thermocycled for 30–35 cycles because of low genomic copy numbers.

Bulk tissues were each placed in 100 µl of QuickExtract DNA Extraction Solution and heated at 65 °C for 15 min and 95 °C for 10 min. 0.5 µl of lysate was used per 25 µl PCR reaction and thermocycled for 25 cycles.

For barcoding for deep sequencing, 1 µl of each unpurified PCR reaction was added to 20 µl of barcoding PCR reaction and thermocycled (95 °C for 3 min; and 10 cycles of: 95 °C for 10 s and 72 °C for 65 s). Amplicons were pooled, the whole sequencing library purified with self-made SPRI beads (9% PEG final concentration), and sequenced on a Miseq (Illumina) for $2 \times 251$ cycles. FASTQ were analyzed with BLAT (with parameters -t=dna -q=dna -tileSize=11 -stepSize=5 -oneOff=1 -repMatch=10000000 -minMatch=4 -minIdentity=90 -maxGap=3 -noHead) and postalignment analyses performed with MATLAB (MathWorks). Alignments due to primer dimers were excluded by filtering off sequence alignments that did not extend >2 bp into the loci from the locus-specific primers. To minimize the impact of sequencing errors, conservative variant calling was performed by ignoring base substitutions and calling only variants that overlapped with a ±30 bp window from the designated Cas9–gRNA cut sites. Negative controls were equally analyzed for baseline sequencing error rates, against which statistical tests were performed.

Off-target sites for *Mstn* gRNAs were predicted using the online CRISPR Design Tool[51] (http://crispr.mit.edu/). Off-target sites were ranked by number of mismatches to the on-target sequence, and deep sequencing was performed on top hits. Sequencing reads were analyzed equally between experimental samples (AAV9–Cas9–gRNAs$^{M3+M4}$) and control samples (AAV9–Cas9–gRNAs$^{TdL+TdR}$) using BLAT. Variant calls were performed for insertions and deletions that laid within a ±15 bp window from potential off-target cut sites.

**Quantitative reverse-transcription PCR (qRT-PCR) for gene expression.** Cells were processed with Taqman Cells-to-Ct kits (Thermo Fisher Scientific No. 4399002) as per manufacturer's instructions, with the modification that each qRT-PCR reaction was scaled down to 25 µl. Taqman hydrolysis probes (Thermo Fisher Scientific) used: *Pd-l1* (Mm00452054_m1), *Fst* (Mm00514982_m1), *Cd47* (Mm00495011_m1), and house-keeping gene *Abl1* (Mm00802029_m1). Gene expression from targeted

genes was normalized to that of *Abl1* (ΔCt). For cell culture experiments, fold-changes were calculated against AAV–Cas9$^C$–VPR-only controls (no-gRNA) ($2^{-\Delta\Delta Ct}$). Basal gene expression percentiles for C2C12 myotubes and GC-1 spermatogonial cells (type B spermatogonia) were retrieved from the Gene Expression Omnibus (GEO) repository (GDS2412 and GDS2390, respectively).

Total RNA from skeletal muscle tissues was extracted via TRIzol. Reverse transcription was conducted with High-Capacity cDNA Reverse Transcription Kit (Applied Biosystems #4368814), and 5 µl of each reaction was used for qRT-PCR in 1× FastStart Essential DNA Probes Master (Roche No. 06402682001). Gene expression from targeted genes was normalized to that of *Abl1* (ΔCt), and fold-changes were calculated against AAV9–turboRFP-only controls ($2^{-\Delta\Delta Ct}$).

**AAV administration in mice.** All AAV experiments *in vivo* were conducted in a randomized and double-blind fashion. The allocation code was unblinded only after analyses were completed. Injections used AAV9–Cas9$^N$–gRNAs:AAV9–Cas9$^C$–P2A–turboGFP and AAV9–Cas9$^N$–gRNAs:AAV9–Cas9$^C$–VPR ratios of 1:1.

3-d-old neonates were each intraperitoneally injected with 4E12, 5E11, or 2.5E11 vector genomes (vg) of total AAV9. Vector volumes were kept at 100 µl. Animals were euthanized via $CO_2$ asphyxia and cervical dislocation 3 weeks following injections. For AAV9–GFP and AAV9–mCherry cotransduction experiments, animals were euthanized 9 d after injection. For qPCR and deep sequencing of whole tissues, samples were taken from the heart body wall, liver, gastrocnemius muscle, olfactory bulb, ovary, testis, and diaphragm.

AAV9–Cas9–VPR–gRNAs were intramuscularly injected at Cas9$^N$–gRNAs:Cas9$^C$–VPR ratio of 1:1, at a total of 4E12 vg. To demarcate transduced tissues, $1 \times 10^{11}$ of AAV9–turboRFP was coadministered in the same mix. Control mice were injected with $1 \times 10^{11}$ of AAV9–turboRFP only, with the final injection mix at the same volume. Animals were euthanized via $CO_2$ asphyxia and cervical dislocation 2 weeks after AAV9–Cas9–VPR–gRNA injection.

For determining AAV- and Cas9- specific immune responses, both tibialis anterior muscles of 11-week-old male C57BL/6 mice were injected with AAV9–Cas9$^N$ and AAV9–Cas9$^C$ ($2 \times 10^{12}$ vg each). For control mice, $4 \times 10^{12}$ of AAV9 vector control (consisting of the same AAV genome with the Cas9 coding sequence removed) was injected per muscle. Vehicle injections were similarly performed. Animals were euthanized via $CO_2$ asphyxia and cervical dislocation 2 weeks after treatment.

**Quantitative PCR (qPCR) for AAV genomic copies in tissues.** Each qPCR reaction consists of 1× FastStart Essential DNA Probes Master (Roche No. 06402682001), 100 nM of each hydrolysis probe (against the AAV ITR and the mouse Acvr2b locus), 340 nM of AAV ITR reverse primer, 100 nM each for all other forward and reverse primers, and 2.5 µl of input tissue lysate. A mastermix was first constituted before splitting 22.5 µl into each well, after which tissue lysates were added. Thermocycling conditions were: 95 °C, 15 min and 40 cycles of 95 °C, 1 min; 60 °C, 1 min. FAM and HEX fluorescence were taken every cycle. AAV genomic copies per mouse diploid genome were calculated against standard curves. For each tissue sample, two repeated samplings were performed for qPCR and deep sequencing,

all on separate days, and the means plotted with s.e.m. qPCR false-positive rates were calculated similarly from two vehicle-injected negative control mice, against which statistical tests were performed.

**Immune cell profiling by FACS.** Muscles were harvested 2 weeks after injections, chopped, and digested with 0.2% collagenase and 0.05% dispase in DMEM for 15 min. Mononuclear cells were separated from the tissue debris using 70 µm nylon sieves and resuspended in Fc blocking solution (1:50; BD Pharmingen) in staining media (1 mM EDTA and 10% FBS in PBS) for 30 min on ice. For experiments using AAV9–GFP as transduction reporter, immune cells were stained with anti-CD45 APC/Cy7 (1:125; BioLegend 103115), anti-CD11b APC (1:125; BioLegend 101211), anti-Ly6G/Gr1 Pacific Blue (1:200; BioLegend 127611), anti-CD3 PE-Cy7 (1:50; BioLegend 100220), anti-CD8a PE (1:50; BD Pharmingen 553033), anti-CD4 PerCP (1:100; BD Pharmingen 561090), anti-CD19 PE-CF594 (1:200; BD clone 1D3 562291) and 7AAD (1:20; eBiosciences 420403) for 20 min on ice. For experiments using AAV9–turboRFP as transduction reporter, all antibodies were the same except that anti-CD8a-FITC (BD clone 53-6.7 553031) was substituted. Flow cytometry was performed on a BD LSR II provided by the Harvard Stem Cell Institute Flow Cytometry Core. Flow cytometry data was collected using FACSDiva software (Becton Dickinson) and analyzed using FlowJo (Tree Star) and MATLAB (MathWorks).

**Cas9 restimulation and TCR-β repertoire sequencing.** Lymphocytes were isolated from both inguinal lymph nodes and one popliteal lymph node per bilaterally injected mouse. Lymph nodes were cut and incubated for 30 min in RPMI + 1 mg/ml collagenase at room temperature (RT). Lymphocytes were released by meshing through 70 µm nylon sieves, washed twice with 1× PBS + 5 mM EDTA, and resuspended in 500 µl of growth media (RPMI 1640 + 10% FBS + 1× Pen–Strep–AmphoB + 50 µM 2-βME). Cell counting was performed on a Countess device (Life Technologies). For Cas9 restimulation experiments, 2.5 µg of recombinant Cas9 (NEB) was incubated with >$10^6$ cells in 500 µl of growth media for 3 d. Experiments were conducted in parallel with wells containing cells without restimulation (i.e., without Cas9 protein). Cellular RNA was extracted using QIAshredder and RNeasy micro (Qiagen). Reverse transcription was performed with SMARTscribe (Clontech), using SMARTNNN template-switching adaptor as described[52]. KAPA HiFi polymerase was used for PCR. Individual RNA molecules were counted based on Unique Molecular Identifiers using MIGEC[53] and aligned with MIXCR[54], and postanalysis was performed with MATLAB (MathWorks). Morisita–Horn indices per exposure condition were calculated by pairwise comparisons among four mice (two animals from electroporation data set and two animals from AAV data set).

**ELISA.** A modified protocol adapted from Wang *et al.*, 2015 (ref. 38) was used. Briefly, recombinant SpCas9 protein (PNA Bio, cat. no. CP01) was diluted in 1× coating buffer (KPL), and 0.5 µg was used to coat each well of 96-well Nunc MaxiSorp Plates (Thermo Scientific) overnight at 4 °C. Plates were washed three times for 5 min with 1× wash buffer (KPL) and blocked with 1% BSA Blocking Solution (KPL) for 1 h at RT. Standard curves were generated using a mouse monoclonal antibody against SpCas9

(Epigentek, clone 7A9, cat. no. A-9000-100) with final concentrations of 0, 1, 2.5, 5, 10, 25, 50, and 100 ng ml$^{-1}$ and in triplicates. Serum samples were added at 1:40 dilution, and plates were incubated for 5 h at 4 °C with shaking. Wells were washed three times for 5 min, and 100 µl of HRP-labeled goat anti-mouse IgG1 (Santa Cruz; diluted 1:4,000 in 1% BSA Blocking Solution) was added to each. After incubating for 1 h at RT, wells were washed four times for 5 min, and 100 µl of ABTS ELISA HRP Substrate (KPL) was added to each. Optical density (OD) at 410 nm was measured using a plate reader (BioTek).

**Fluorescent immunoassay.** To determine antibody specificity and class switching, serum levels of AAV9-specific IgM, IgG, and IgG2a from AAV9-treated mice were compared to those from vehicle-injected control mice. AAV9 viruses (1E9 vg) were coated on each well of a 96-well PVDF MaxiSorp plate for 1 h in 1× TBST, followed by 1 h of blocking in 1× TBST + 3% BSA. After three washes with 1× TBST, 1:100 diluted mouse serum was applied at 25 µl per well, for 1 h. After three washes with 1× TBST, 1:200 diluted anti-mouse secondary antibodies were added (goat anti-mouse IgG-CF633 (Biotium 20120), goat anti-mouse IgG2a-CF594 (Biotium 20259), and goat anti-mouse IgM-Dy550 (Pierce PISA510151)), and incubated for 1 h. Wells were then washed five times with 1× TBST, and fluorescence readings in 100 µl of 1× TBS were taken via a plate reader. All steps were conducted at RT. To account for autofluorescence from sera, fluorescence readings were normalized against that from wells treated similarly except for the exclusion of secondary antibodies.

**Epitope mapping by M13 phage display.** M13KE genome was amplified by PCR, with one end terminating with the pIII peptidase cleavage signal and the other end terminating with a 4× Gly linker followed by the mature pIII. Cas9 and AAV9 VP1 capsid coding sequence PCR products were each randomly fragmented with NEBNext dsDNA Fragmentase until about 50–300 bp. Purified fragments were treated with NEBNext End-Repair Module. After DNA purification, fragments were blunt-ligated into the M13KE PCR product overnight at 16 °C. The entire ligation reaction was purified and transformed into ER2738 (Lucigen) at 200 ng per 25 µl of bacteria with electroporation conditions of 10 µF, 600 Ω, and 1.8 kV. After 30 min recovery in SOC media, the culture was amplified by combining with 20 ml of early-log ER2738 culture. After 4 h, the culture supernatant was collected and incubated to a final concentration of 3.33% PEG-8000 and 417 mM of NaCl overnight at 4 °C. M13 phage was pelleted and resuspended in 2 ml of TBS. Phage titers were determined by LB/IPTG/X-gal blue–white plaque counting, averaging >1 ×10$^{11}$ pfu/µl. For Ig:phage pulldown, 20 µl of each phage library was incubated with 5 µl of mouse serum or titrated amount of purified antibody controls (7A9 (Novus Bio), Guide-IT (Clontech), bG15 (Santa Cruz), bS18 (Santa Cruz), bD20 (Santa Cruz), and nonbinding mouse IgG isotype control (Santa Cruz)) and made up to 50 µl with TBST for 1 h at RT. For each reaction, 25 µl of Protein A/G magnetic beads (Millipore PureProteome) was first washed twice with TBST, resuspended to 10 µl, and added to the reaction for additional 30 min incubation. The beads were then washed five times with TBST, and captured Ig:phage was eluted with 100 µl of 200 mM glycine–HCl, pH 2.2, 1 mg/ml BSA for 8 min. The eluant was neutralized with 15 µl of 1 M Tris–HCl,

pH 8.5. 5 µl of captured phage display eluant was used per PCR reaction, with 20 cycles of spacer amplification and 10 cycles of barcoding, and it was sequenced on a Miseq (Illumina). Each serum sample was processed for technical replication on separate days. Differential binding of phage was determined using DESeq2 (ref. 55) in R[56], with all Cas9-unexposed ($n = 16$ animals) or AAV-unexposed ($n = 16$ animals) samples as appropriate controls for nonspecific binding. Alignments and further analyses were performed with MATLAB (MathWorks). Visualization of epitopes on Cas9 (PBD ID: 4CMP, chain A) and AAV9 VP3 (PBD ID: 3UX1) structures was conducted with Pymol. Phenotypic data of double-alanine AAV9 mutants were obtained from ref. 35, with mutant viral blood persistency calculated as the difference in blood viral levels 72 h and 10 min postinjection (both normalized to that of wildtype AAV9, with 0 denoting wildtype phenotype and negative values denoting loss of blood persistency). Mutant tropism was represented by 'Phenotypic Difference' values as described[35]. Solvent-accessibility surface area (sasa) ratios for AAV9 capsid (PDB ID: 3UX1; ref. 57) were first calculated as described[58], and the final sasa ratio per residue calculated as the mean from a ±5 bp sliding window centered on the residue.

**Total mRNA sequencing.** 1 µg of TRIzol-extracted RNA from muscle tissues or draining lymph node tissues was enriched for polyA-tailed mRNA and processed with NEBNext Ultra Directional RNA Library Prep Kit (New England BioLabs), followed by sequencing on a NextSeq sequencer (Illumina), giving ~30 million reads per sample. Reads were aligned to the mm10 reference genome and FPKM quantified with the Cufflinks workflow[59], with differential expression tested with Cuffdiff[60]. GO-terms network was visualized with ClueGO[61] Cytoscape[62] plug-in. Immune cell reference transcriptomes were downloaded from the ImmGen database. DCQ deconvolution was conducted as described[36] in R[56].

**Histology and immunofluorescence staining.** Mouse organs and tissue samples were dissected, fixed in 4% paraformaldehyde in 1× DPBS for 1.5 h, followed by three 5 min washes with 1× DPBS. Samples were immersed in 30% sucrose until submersion, embedded in O.C.T. compound (Tissue-Tek), frozen in liquid-nitrogen-cold isopentane, and cryosectioned on a Microm HM550 (Thermo Scientific). Skeletal muscles were sectioned to a thickness of 12 µm, while the liver and heart were sectioned at 20 µm.

For immunofluorescence, tibialis anterior (TA) muscle sections were blocked in 1× PBST + 3% BSA for 1hr at RT and immunostained with primary antibodies at RT for 1 h, followed by three washes with PBS/T. Slides were then incubated with secondary antibodies at RT for 1 h, followed by three washes with PBS/T.

Anti-mouse laminin (Abcam ab14055) was used at 1:400, followed by 1:250 of secondary antibody goat anti-chicken IgY Alexa Fluor 555 (Life Technologies A-21437). Anti-CD45 APC (BioLegend 103112) was used at 1:100. Goat anti-mouse IgG-CF633 (Biotium 20120) and goat anti-mouse IgM-Dy550 (Pierce PISA510151) were used at 1:200 to detect endogenous mouse antibodies.

Anti-mouse IL-2 and perforin antibodies were used at 1:100 (Santa Cruz sc-7896 and sc-9105, respectively), followed by 1:200 of secondary anti-rabbit CF633 (Biotium). Immunostaining was conducted on three separate days, with a mix of electroporated, AAV-injected, and control tissue samples each time.

Immunostained slides were mounted with mounting media containing DAPI (Vector Laboratories, H1500).

**Western blot.** Muscles were harvested 2 weeks after AAV injections or plasmid electroporation. ~10 mm$^3$ tissue clippings were flash frozen in liquid nitrogen, followed by lysis in 300–500 µl of T-PER Tissue Protein Extraction Solution (Thermo Scientific) supplemented with 1× Complete Protease Inhibitor (Roche) and homogenized in gentleMACS M tubes (Miltenyi Biotec). 10–15 µl of each tissue lysate was run on 8% Bolt Bis-Tris Plus gels (Life Technologies) in 1× Bolt MOPS SDS running buffer at 165 V for 50 min. Protein transfer was performed with iBlot (Life Technologies) onto PVDF membranes, using program 3 for 13 min. Western blots were conducted with 1:200 of anti-Cas9 Guide-IT polyclonal antibody (Clontech 632607), 1:400 of anti-Gapdh polyclonal antibody (Santa Cruz sc-25778), and 1:2,500 of anti-rabbit IgG-HRP secondary antibody (Santa Cruz sc-2004), using an iBind device (Life Technologies). Stained membranes were developed with SuperSignal West Femto Maximum Sensitivity Substrate (Thermo Scientific) and imaged on Chemidoc MP (Bio-Rad). Band intensities were quantified with ImageJ (NIH).

**Immunosuppression.** FK506 was dissolved in 100% DMSO, and the stock solution was further diluted 1:100 in vehicle for final concentrations of 1% DMSO, 10% Cremophor (Sigma-Aldrich, C5135), and 1× PBS. Mice were injected daily with 5 mg/kg (body weight) of FK506, with the first injection commencing 1 d before *in vivo* electroporation.

For Cas9-gRNAs-injected muscles, a mix of 30 µg of minicircle–SMVP–Cas9, 15 µg of pCAG–GFP, and 30 µg total of pCRII–U6–gRNA plasmids was injected. 30 µg of minicircle–SMVP–Cas9 was injected for Cas9-only injections, 30 µg of pCRII–U6–gRNA plasmids for gRNAs-only injections, 15 µg of pCAG–GFP for GFP-only injections. Four mice were injected per condition.

For body weight measurements, 2-month-old mice were injected with 5 mg/kg/d of FK506 or vehicle for 2 weeks. Three male C57BL/6 mice were injected per condition.

**Imaging and analyses.** Confocal images were taken using a Zeiss LSM780 inverted microscope. For live-cell imaging, each image consists of 3× z-stacks (7 µm intervals) and 2 × 2 tiles. For muscle sections, 3× z-stacks (7 µm intervals) were used. For liver and heart sections, 4× z-stacks (10 µm intervals) were used. Tiling was used to image entire samples, followed by stitching. Stacked fluorescence images were projected by maximum intensity with Zen 2011 (Carl Zeiss).

Epifluorescence images were taken with an Axio Observer D1 (Carl Zeiss) or Axio Observer Z1 (Carl Zeiss).

For cotransduction analysis after AAV9–GFP and AAV9–mCherry administration, pixels that contained both GFP and mCherry fluorescence intensities above the background thresholds were identified, and the lower intensity values from either channel were used to populate a merged image. All other pixels in the merged image were set to null.

Centrally nucleated myofibers were quantified from whole section images with CellProfiler[63], and random inserts were counted manually.

Whole organ images were taken on an SMZ1500 (Nikon) fluorescence dissection stereomicroscope equipped with a SPOT RT3 camera (Diagnostic Instruments) for an imaging area of 16 mm by 12 mm, with 3 s exposure for the liver and 4 s exposure for the heart, muscle, brain, and gonads. All images were acquired with a gain setting of 8 using the SPOT imaging software (Diagnostic Instruments, Sterling Heights, MI). Images for each organ were inverted and thresholded equally across animals.

Images were analyzed with ImageJ (NIH), CellProfiler[63], and MATLAB (MathWorks).

**Availability of software and scripts.** Software is cited by primary literature and available on online repositories. All custom scripts used in the study will be readily provided upon request.

44. Kay, M.A., He, C.Y. & Chen, Z.Y. A robust system for production of minicircle DNA vectors. *Nat. Biotechnol.* **28**, 1287–1289 (2010).
45. Balazs, A.B. *et al.* Antibody-based protection against HIV infection by vectored immunoprophylaxis. *Nature* **481**, 81–84 (2011).
46. Matsuda, T. & Cepko, C.L. Electroporation and RNA interference in the rodent retina *in vivo* and *in vitro*. *Proc. Natl. Acad. Sci. USA* **101**, 16–22 (2004).
47. Grieger, J.C., Choi, V.W. & Samulski, R.J. Production and characterization of adeno-associated viral vectors. *Nat. Protoc.* **1**, 1412–1428 (2006).
48. Zolotukhin, S. *et al.* Recombinant adeno-associated virus purification using novel methods improves infectious titer and yield. *Gene Ther.* **6**, 973–985 (1999).
49. Aurnhammer, C. *et al.* Universal real-time PCR for the detection and quantification of adeno-associated virus serotype 2-derived inverted terminal repeat sequences. *Hum. Gene Ther. Methods* **23**, 18–28 (2012).
50. Aihara, H. & Miyazaki, J. Gene transfer into muscle by electroporation *in vivo*. *Nat. Biotechnol.* **16**, 867–870 (1998).
51. Hsu, P.D. *et al.* DNA targeting specificity of RNA-guided Cas9 nucleases. *Nat. Biotechnol.* **31**, 827–832 (2013).
52. Mamedov, I.Z. *et al.* Preparing unbiased T-cell receptor and antibody cDNA libraries for the deep next generation sequencing profiling. *Front. Immunol.* **4**, 456 (2013).
53. Shugay, M. *et al.* Towards error-free profiling of immune repertoires. *Nat. Methods* **11**, 653–655 (2014).
54. Bolotin, D.A. *et al.* MiXCR: software for comprehensive adaptive immunity profiling. *Nat. Methods* **12**, 380–381 (2015).
55. Love, M.I., Huber, W. & Anders, S. Moderated estimation of fold change and dispersion for RNA-seq data with DESeq2. *Genome Biol.* **15**, 550 (2014).
56. R Development Core Team. *A language and environment for statistical computing* (R Foundation for Statistical Computing, 2014).
57. DiMattia, M.A. *et al.* Structural insight into the unique properties of adeno-associated virus serotype 9. *J. Virol.* **86**, 6947–6958 (2012).
58. Mandell, D.J. *et al.* Biocontainment of genetically modified organisms by synthetic protein design. *Nature* **518**, 55–60 (2015).
59. Trapnell, C. *et al.* Transcript assembly and quantification by RNA-Seq reveals unannotated transcripts and isoform switching during cell differentiation. *Nat. Biotechnol.* **28**, 511–515 (2010).
60. Trapnell, C. *et al.* Differential analysis of gene regulation at transcript resolution with RNA-seq. *Nat. Biotechnol.* **31**, 46–53 (2013).
61. Bindea, G. *et al.* ClueGO: a Cytoscape plug-in to decipher functionally grouped gene ontology and pathway annotation networks. *Bioinformatics* **25**, 1091–1093 (2009).
62. Shannon, P. *et al.* Cytoscape: a software environment for integrated models of biomolecular interaction networks. *Genome Res.* **13**, 2498–2504 (2003).
63. Carpenter, A.E. *et al.* CellProfiler: image analysis software for identifying and quantifying cell phenotypes. *Genome Biol.* **7**, R100 (2006).